Supporting Information to

Operando Electrical Conductivity and Complex Permittivity Study on Vanadia Oxidation Catalysts

Anna M. Wernbacher,[1] Maik Eichelbaum,[1] Thomas Risse,[2] Sébastien Cap,[1]

*Annette Trunschke,[1,] * and Robert Schlögl[1,3]*

[1]Department of Inorganic Chemistry, Fritz-Haber-Institut der Max-Planck-Gesellschaft, Faradayweg 4-6, 14195 Berlin, Germany

[2]Institute of Chemistry and Biochemistry - Physical and Theoretical Chemistry, Freie Universität Berlin, Takustraße 3, 14195 Berlin, Germany

[3]Department of Heterogeneous Reactions, Max-Planck-Institut für Chemische Energiekonversion, Stiftstraße 34-36, 45470 Mülheim a. d. Ruhr, Germany

wernbacher@fhi-berlin.mpg.de

Maik.Eichelbaum@bmbf.bund.de

trisse@zedat.fu-berlin.de

sebastiencap@fhi-berlin.mpg.de

trunschke@fhi-berlin.mpg.de

acsek@fhi-berlin.mpg.de

Sample Characterization

A description of the VPP sample preparation can be found elsewhere.[1] The catalyst was pelletized with 1 wt-% graphite and activated in an *n*-butane oxidation gas feed (2% *n*-butane / 3% H_2O in air, 1 ppm triethylphosphate) for about 500 h after a thermal treatment (in air and in N_2/H_2O 1:1), see Eichelbaum *et al.*[1] In the *operando* MCPT measurements a sieve fraction of 100 to 200 µm of the crushed catalyst pellets was investigated.

X-ray fluorescence (XRF) measurements were performed on a Bruker Pioneer S4 Spectrometer. The V_2O_5 sample (SN 22054) was found to consist of 100 wt-% V_2O_5 and the VPP sample (SN 12831) showed 56.4 wt-% V_2O_5 and 43.6 wt-% P_2O_5 (P/V atomic ratio of 1.0).

X-ray powder diffraction (XRPD) measurements were conducted on the Bruker AXS D8 Advance II theta/theta diffractometer (Ni filtered Cu Kα radiation). The powder diffractograms of the VPP samples (SN 12831 and 10449) are shown in Figure S1 together with the one of a VPP sample (SN 22698) after the *operando* MCPT conductivity measurements, where the main reflections of the vanadyl pyrophosphate crystal structure (ICSD 280777) are indexed. The corresponding powder diffractograms of the fresh (SN 22054) and used V_2O_5 samples after the operando MCPT measurements (SN 24399) and the ICSD entry of α-V_2O_5 (60767) is shown in Figure S2 together with the assignment of the main reflections.

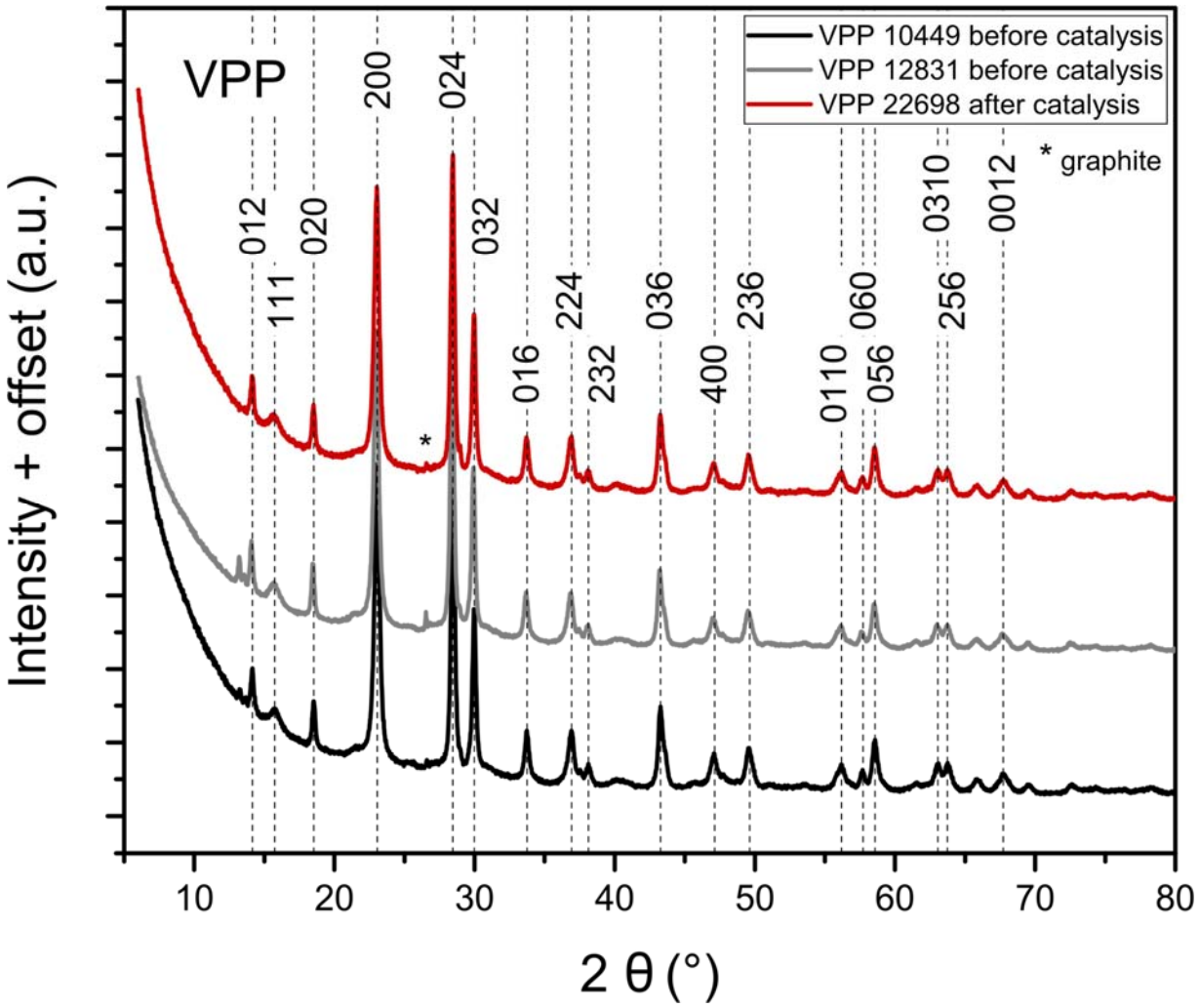

Figure S1. X-ray powder diffractograms of VPP samples (SN 12831 and 10449) and of VPP sample after MCPT conductivity measurements (SN 22698).

The peaks below 2θ of 14° in the XRD pattern of the unpretreated VPP samples 12831 and 10449 in Figure S1 may be ascribed to the hydrated phases $(VO)(HPO_4)(H_2O)_4$ and $(VO)_3(PO_4)_2 \cdot 6H_2O$.

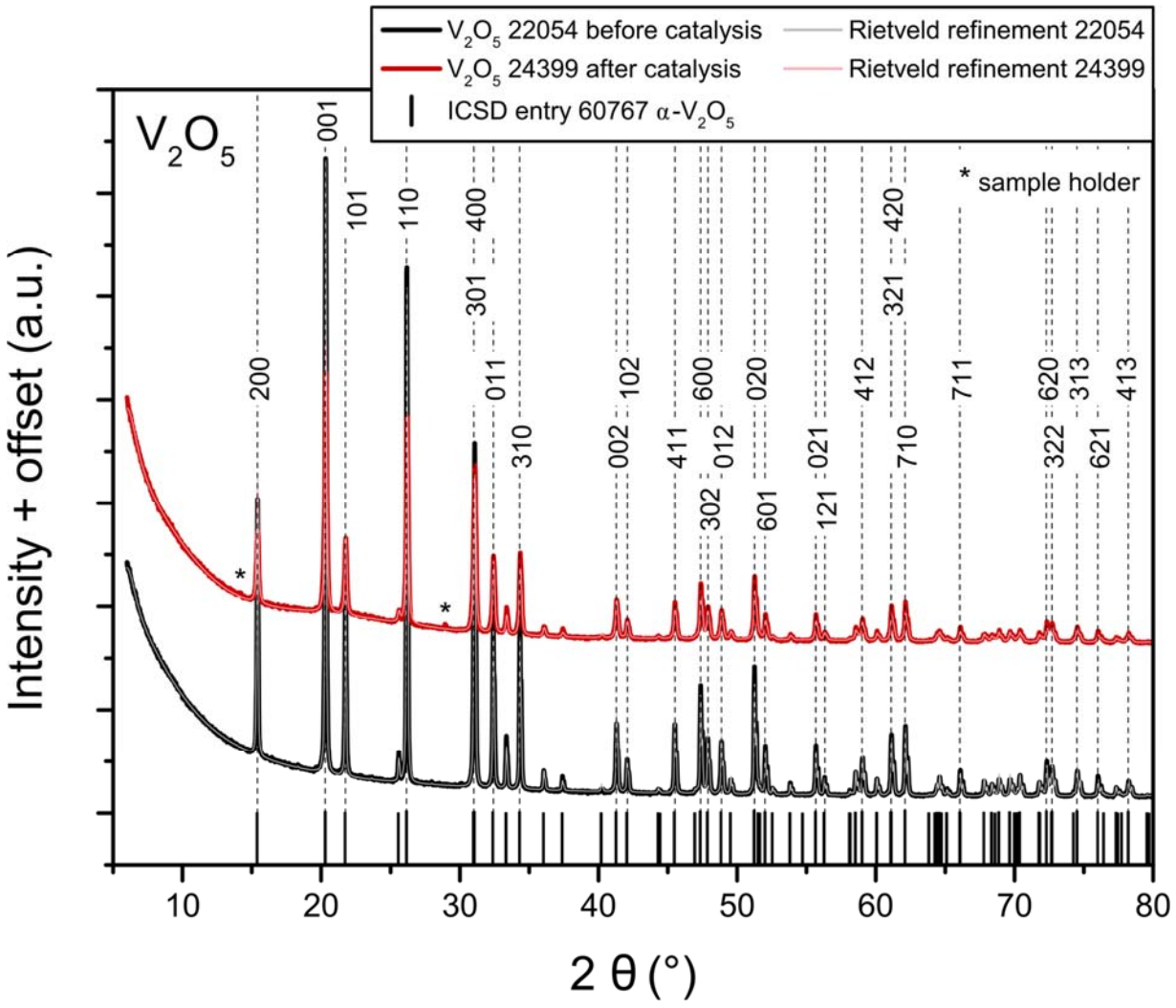

Figure S2. X-ray powder diffractograms of V_2O_5 sample (SN 22054) and of V_2O_5 sample after MCPT conductivity measurements (SN 24399). The Rietveld fit of the two samples is shown in gray and in light red on top of the measured diffractograms, respectively.

High-resolution transmission electron microscopy (TEM) imaging of the VPP sample (Figure S3 (a)) was performed on the JEOL JEM-ARM200F, operated at 200 kV acceleration voltage, using a low dose due to a beam induced sample transformation (electron dose of about 2 $\mu A/cm^2$). In the beginning all VPP particles were crystalline with a very small amorphous part (ca. 1 - 2 nm) on top, which started to grow with prolonged time under the electron beam until

the particles became completely amorphous. The V_2O_5 sample likewise showed beam damage effects with an oxygen loss and a transformation to lower vanadium oxides starting from the surface (Figure S3 (b), JEOL JEM-ARM200F).

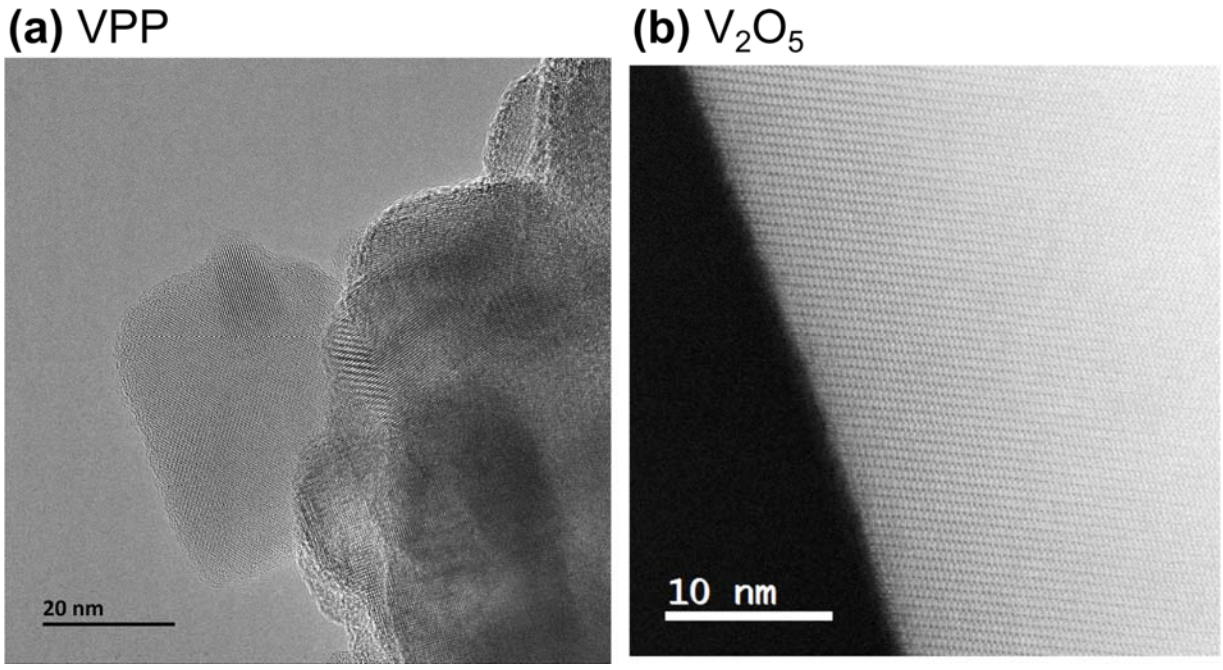

Figure S3. (a) High resolution TEM micrograph of the VPP sample (SN 12831, electron dose ~2 µA/cm^2); **(b)** annular dark field (ADF) STEM micrograph of the V_2O_5 sample (SN 22054).

MCPT Conductivity and Permittivity

Correlations between Permittivity/Conductivity and Catalytic Performance

The electrical conductivity and complex permittivity of the vanadium oxide-based catalysts V_2O_5 and vanadyl pyrophosphate (VPP) were investigated during the oxidation of *n*-butane (2% C_4H_{10} / 20% O_2 in N_2) at 400 °C with total gas flows ranging from 2 to 30 ml/min. The response of VPP to different contact times (total gas flows) was tested in three different microwave

resonators operating at resonant frequencies from ~3 to 10 GHz using the TM_{010} and TM_{020} modes. Furthermore, two different VPP samples batches (no. 12831 and no. 10449) were investigated. The electric and magnetic field distributions of the two modes are depicted in Figure S4.

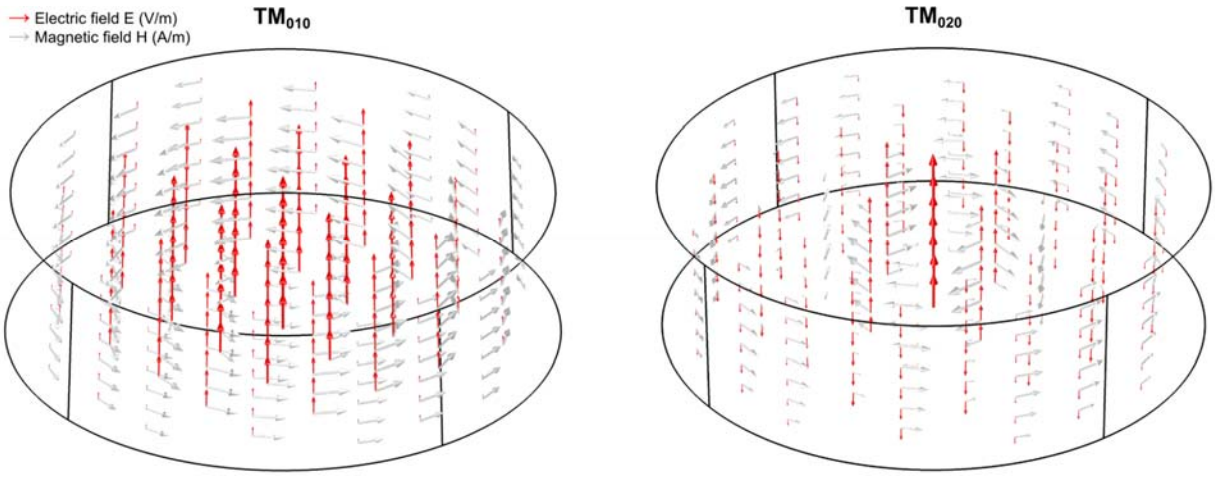

Figure S4. Numerically simulated electric field (red arrows) and magnetic field (light gray arrows) inside a cylindrical microwave cavity (left: TM_{010} mode; right: TM_{020} mode) with FEM package COMSOL Multiphysics 5.1, RF module.

The results of the repeated contact time variation experiments of VPP are shown in Figure S5 to Figure S7. The conductivity changes induced by different reactant conversions in one gas feed were found to be much less pronounced than the changes in between different gas feeds. In order to resolve the small changes of the less conductive VPP at increasing *n*-butane conversion, the measurements had to be conducted in smaller microwave resonators, which exhibit a larger sample/resonator volume ratio (cf. Figure S5 (c)) and hence a greater perturbation in addition to a higher resonant frequency. Furthermore, the second mode TM_{020} was found to be stable and sensitive to changes of the sample. The absolute conductivity could be influenced the frequency,

which should be considered in a comparison of V_2O_5 with VPP in these contact time variation experiments since V_2O_5 was measured at ~3 GHz. Nevertheless, the trends of the conductivity changes with *n*-butane conversion (i.e. at different contact times) can be compared in any case.

The conductivity response of the two VPP sample batches in the contact time variation experiments is presented in Figure S5 (a) as time on stream plot in 2% *n*-butane / 20% oxygen in N_2 at 400 °C. The electrical conductivity of VPP was not found to be significantly influenced by the frequency showing an average value of $2.0 \cdot 10^{-2}$ S/m in all the microwave resonators and modes, which were measured over a time period of two years in the *in situ* MCPT setup. This value is also in good agreement with the reported $1.7 \cdot 10^{-2}$ S/m of VPP at 400 °C in 3% propane / 6% oxygen in N_2 (5 GHz, TM_{010} mode),[2] in particular given the expected lower conductivity of the p-type semiconductor VPP in a more reducing gas feed. This finding suggests that also the absolute conductivity of VPP from the contact time variation experiments can be compared to the one of the much more conductive V_2O_5. Still, a seemingly lower conductivity of VPP was observed in one single measurement at 7 GHz shown in gray in Figure S5 (a), which may be attributed to the usage of a "wrong" microwave mode given the close vicinity of other modes to the intended TM_{020} mode.

In order to show the small conductivity changes of VPP at different contact times, an offset plot of the conductivity as a function of time on stream at 400 °C is presented in Figure S5 (b).

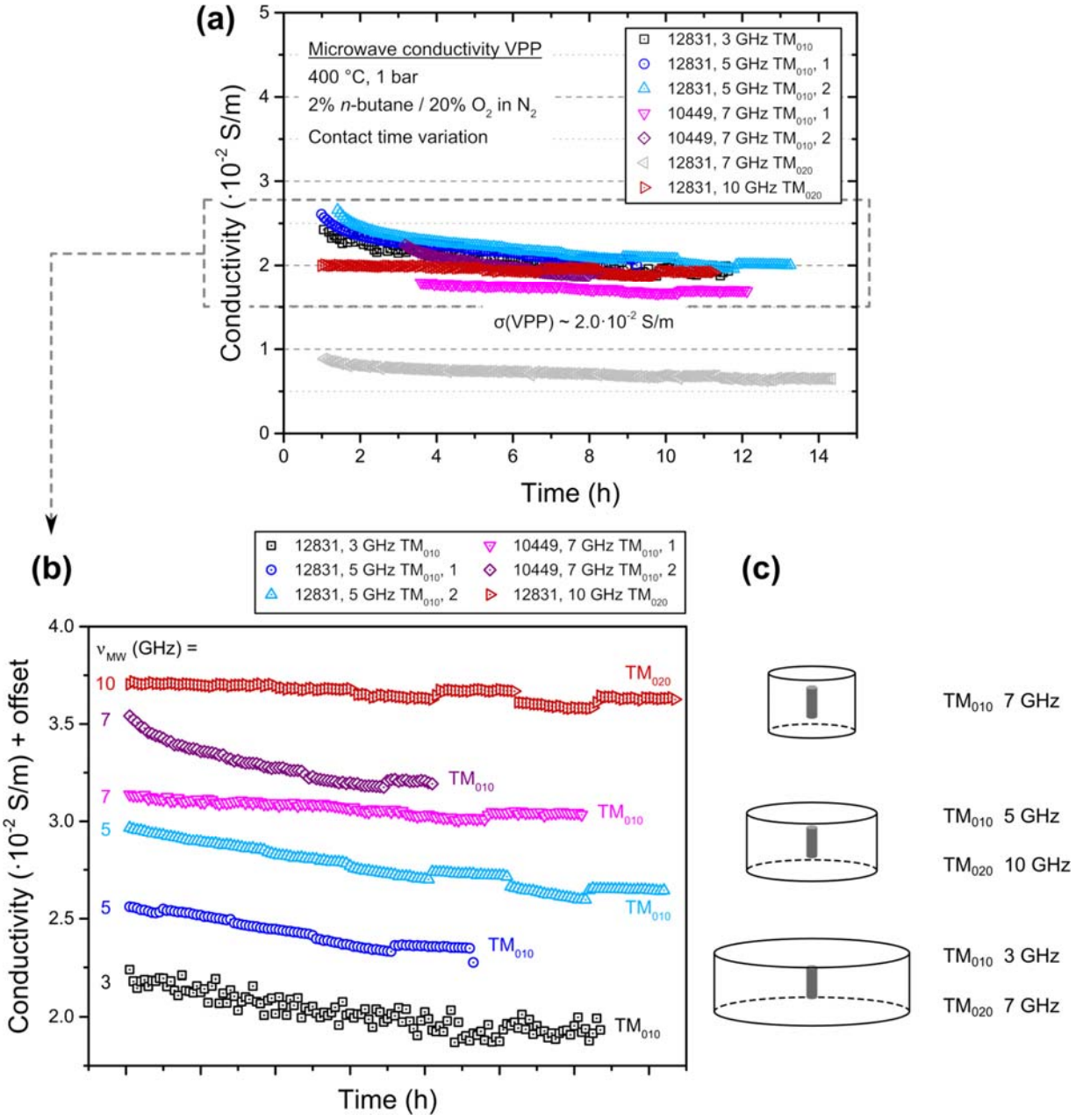

Figure S5. (a) MCPT contact time variation experiments of VPP at 400 °C in 2% *n*-butane / 20% oxygen in N_2 measured in three different resonators (increasing sample/resonator volume ratio and resonant frequency) using two microwave modes (TM_{010} and TM_{020}) and two different VPP sample batches (no. 12831 and no. 10449); **(b)** offset plot of the conductivity measurements in order to show the small changes at different contact times.

It can be seen in Figure S5 (b) that hardly any conductivity response could be detected in the ~3 GHz resonator, which exhibits the smallest sample/resonator volume ratio as shown in Figure S5 (c). The best signal stability and resolution of the conductivity changes was found in a smaller microwave cavity operating at ~10 GHz (TM_{020} mode), which was therefore chosen for a further analysis of the correlation between conductivity and catalytic performance.

Figure S6 shows the response of the real part of the permittivity ε' of VPP in the contact time variation experiments. The inset, which is highlighted in gray, is a magnification of the first three measurements in the 3 GHz and 5 GHz resonators.

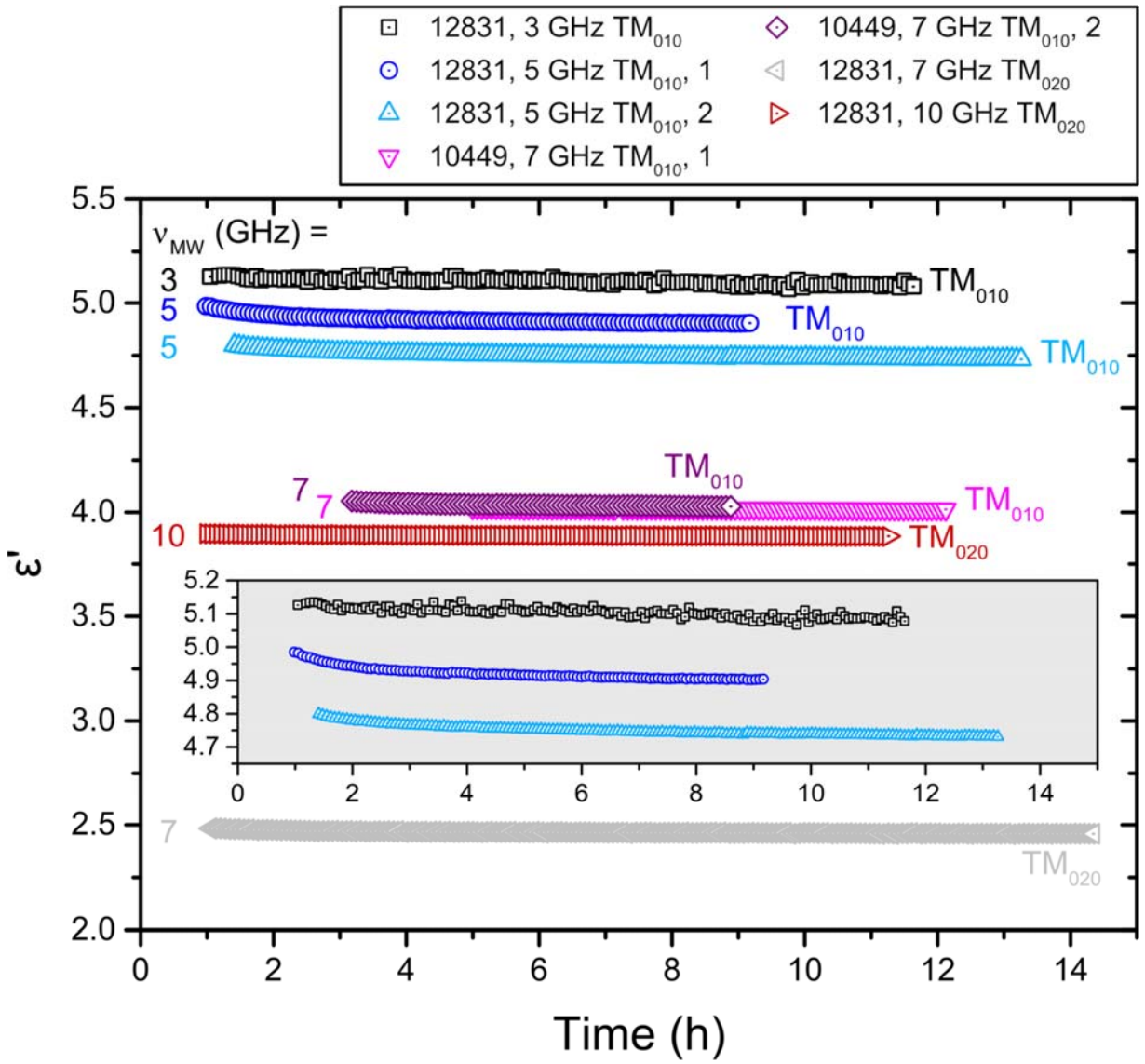

Figure S6. Real part of permittivity of VPP from MCPT contact time variation experiments in Figure S5: measurements using TM_{010} and TM_{020} modes in different resonators of the VPP samples no. 12831 and no. 10449 at 400 °C in 2% *n*-butane / 20% O_2 in N_2.

Interestingly, the real part of the permittivity of VPP showed no changes at different *n*-butane conversions as opposed to the response of ε' of V_2O_5 in the contact time variation experiments. This observation holds generally true, as can be seen in Figure S6 for the two VPP sample batches (no. 12831 and no. 10449) in the different resonators from ~3 to 10 GHz and using the

TM_{010} and TM_{020} modes. In addition, there seems to be an increase of ε' with increasing operating frequency, disregarding again the 7 GHz "TM_{020}" measurement shown in gray.

The catalytic performance of VPP recorded with online GC during the MCPT contact time variation experiments is shown in Figure S7 in terms of a selectivity-conversion plot.

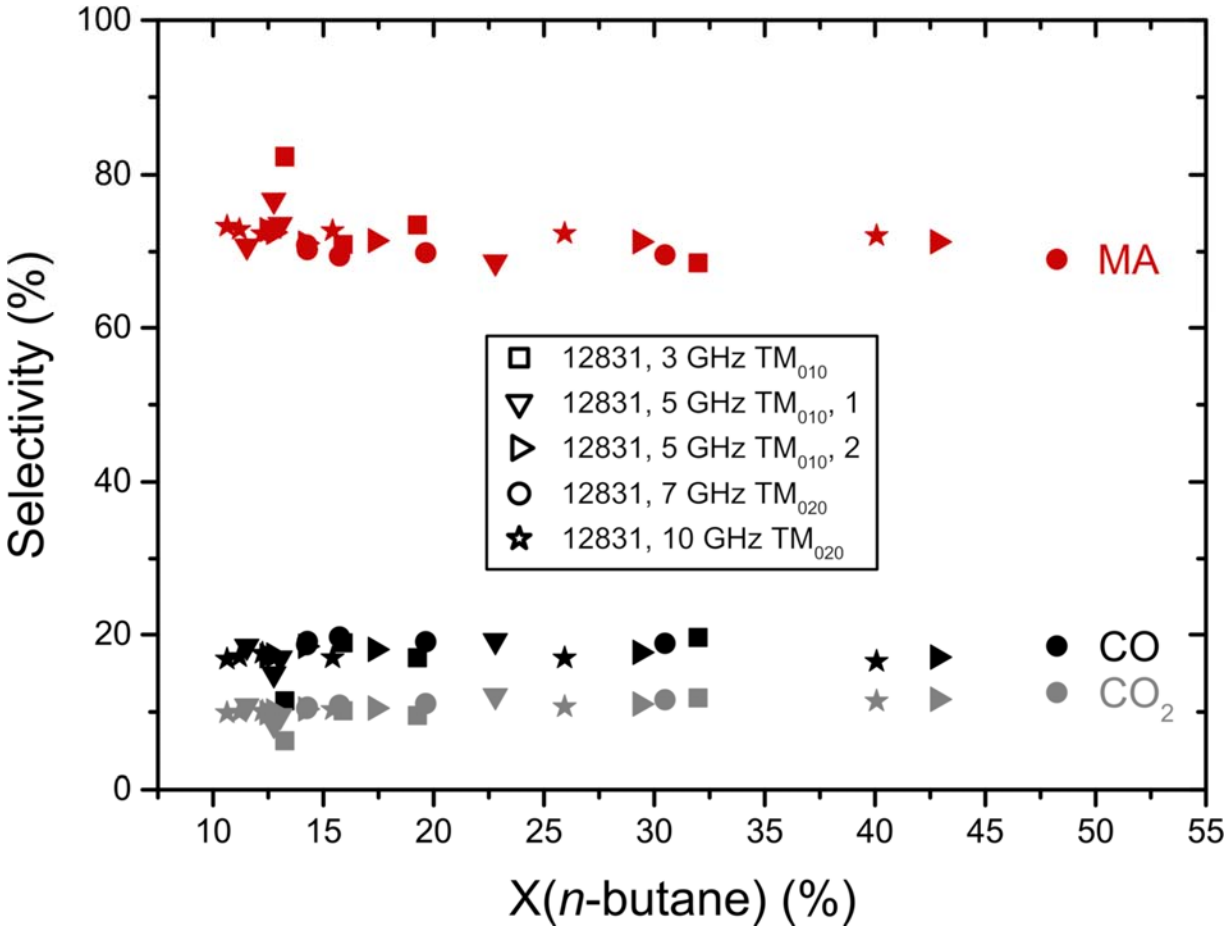

Figure S7. Selectivity-conversion (S-X) plot from MCPT contact time variation experiments in Figure S5: VPP sample no. 12831 at 400 °C in 2% *n*-butane / 20% O_2 in N_2.

A stable average maleic anhydride selectivity of about 72% was observed over a comparatively wide range of *n*-butane conversions, together with selectivities of approx. 18% and 10% to CO and CO_2, respectively.

Redox Properties

The V_2O_5 sample showed reversible conductivity changes in different gas feeds (2% *n*-butane / 20% O_2 in N_2 ; 20% O_2 in N_2 ; 100% N_2 ; 2% *n*-butane / 20% O_2 in N_2; "redox response"). The oxidation of V_2O_5 in the 20% oxygen in nitrogen gas feed, which lead to a conductivity decrease due to a consumption of charge carriers,[3]

$$O_2(\text{ads}) + 2\,V_O^{\bullet\bullet} + 4\,e' \rightarrow 2\,O_O^x \qquad (1)$$

proceeded slower and after two hours no steady state of was reached. This was also reported in the literature,[4] where a combination of a fast surface oxidation process and a slower process involving the healing of oxygen vacancies V_O was suggested (see above in Eq. (1)).[4] In line with this interpretation, the conductivity and permittivity response can be described by an exponential decay in the O_2/N_2 gas feed with two rate constants.

The 100% nitrogen feed acted slightly reducing compared to the O_2/N_2 gas feed, which may be due to oxygen loss at 400 °C in an O_2-free gas atmosphere. The following treatment of V_2O_5 in the reaction gas feed proved the reversibility and stability of the catalyst.

In non-stoichiometric oxides like V_2O_5 that are prone to oxygen loss ("V_2O_{5-x}"), for instance in reducing gas atmospheres or under ultra-high vacuum at elevated temperatures,[3, 5-8] the oxygen vacancies are believed to be a source of charge carriers (electrons) and are thus related to the electrical conductivity.[3, 9-10] The remaining electrons were shown to be localized at vanadium centers (filled V 3d levels) in the neighborhood of the oxygen vacancies or increasingly freed at

higher temperatures.[8, 10-15] Perlstein, however, stated that there is probably no simple relation between the oxygen vacancies and the electrical conductivity in vanadium pentoxide.[16] Similarly, it may be assumed that the situation in vanadyl pyrophosphate is likewise more complicated.

The absorption below 500 to 600 nm in the spectra of V_2O_5 in Figure S8 (a), which has a band gap of about 2.0 to 2.2 eV,[17-18] is due to O^{2-}–V^{5+} ligand-to-metal charge transfer (LMCT) transitions.[19-20] In addition to the CT transition, also transitions from V^{4+} ($3d^1$) can contribute to the spectra of partially reduced V_2O_5.[11, 20] In the literature, the NIR absorption of V_2O_5 is attributed to transitions from $3d^1$ states and their intensity increases with increasing amount of V^{4+}.[11] This can be seen in the present study on V_2O_5 by the increase of the absorption before the CT edge in the region of the "baseline" in the reducing reaction gas feed, see the inset in Figure S8 (a). In the oxidizing O_2/He gas feed, a decrease of the intensity in this region was observed, which indicates a decrease in the number of the V^{4+} centers.

This effect was also shown in a study on supported V_2O_5 on ZrO_2 in the literature, where an increasing intensity below the absorption edge with increasingly reducing gas feeds at 300 °C was clearly demonstrated,[20] see also the work by Heine *et al.*[4] on V_2O_5 in *n*-butane- and O_2-containing gas atmospheres.[4]

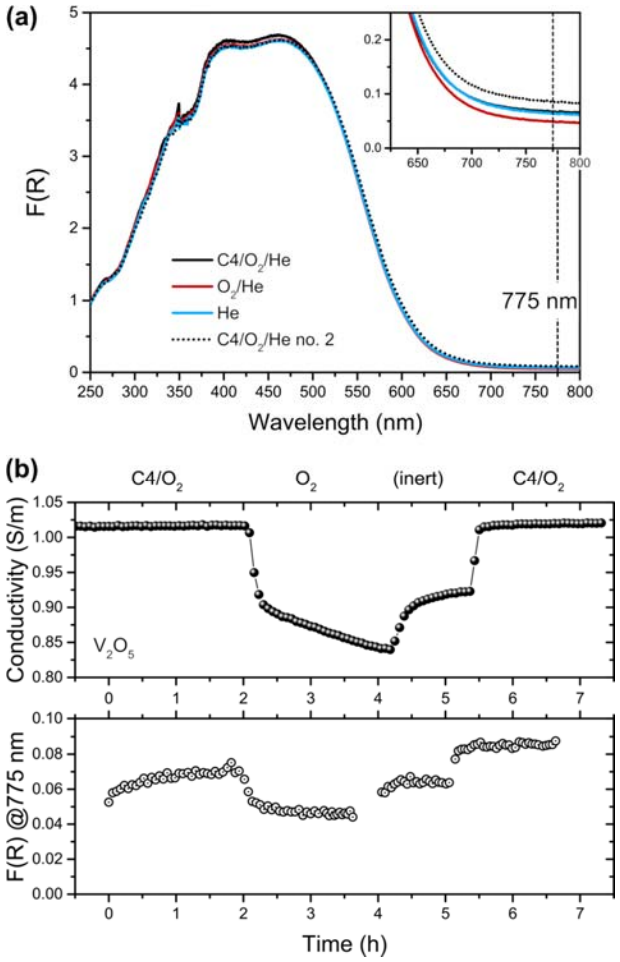

Figure S8. (a) DR-UV-Vis spectra of V_2O_5 recorded at 400 °C in different gas feeds (average spectra); **(b)** comparison of MCPT conductivity and absorption at 775 nm as time on stream plots in different gas feeds.

In Figure S8 (b) the similarity of the MCPT conductivity changes in the different gas feeds at 400 °C to the changes in the intensity at 775 nm in the DR-UV-Vis spectra of V_2O_5 can be seen. Hence, both the increased absorption (Kubelka-Munk function F(R)), which was attributed to V^{4+} centers, and the MCPT conductivity are caused by the same effects, i.e. an increased reduction of the V_2O_5 sample leading to a higher electrical conductivity of the n-type semiconductor in the reaction gas feed. This correlation between the DR-UV-Vis measurements

and the MCPT experiments strongly supports the interpretation of the response of the conductivity and of ε'' as due to a change in the number of charge carriers.

The DR-UV-Vis experiments were also extended to the p-type VPP, which has a bulk vanadium oxidation of +4. The DR-UV-Vis spectra of VPP are presented in Figure S9 (a) at 400 °C. Here, the average spectra in the respective gas feeds are shown and the assignment of the bands according to literature is indicated in the figure. Furthermore, the absorption of VPP at 385 nm (in terms of the Kubelka-Munk function F(R)) is compared to the electrical conductivity response in Figure S9 (b).

VPP showed the same redox behavior as V_2O_5 in the different gas feeds, except that the conductivity increased in the oxidizing gas feeds (increase of the majority charge carries, i.e. holes)[21]

$$O_2(\text{ads}) + 2\,V_O^{\bullet\bullet} \;\rightarrow\; 2\,O_O^x + 4\,h^{\bullet} \qquad (2)$$

and decreased upon reduction. The trapping of a hole by lattice oxygen can lead to the creation of a reactive O^- species (or "$O_O^{\bullet}$").[21-22]

$$O_O^x + h^{\bullet} \rightleftharpoons O_O^{\bullet} \;\;/\;\; V^{5+} + O^{2-} \rightleftharpoons V^{4+} + O^{-} \qquad (3)$$

As was discussed above for V_2O_5, the reduction of VPP in $C_4H_{10}/O_2/N_2$ also proceeded faster than the oxidation in O_2/N_2, where no steady state was reached after two hours.

The conductivity of VPP stabilized in the subsequently applied 100% nitrogen gas feed, which stopped the ongoing oxidation. The initial conductivity of $2 \cdot 10^{-2}$ S/m was then reached again by the treatment of VPP in the last reaction gas feed.

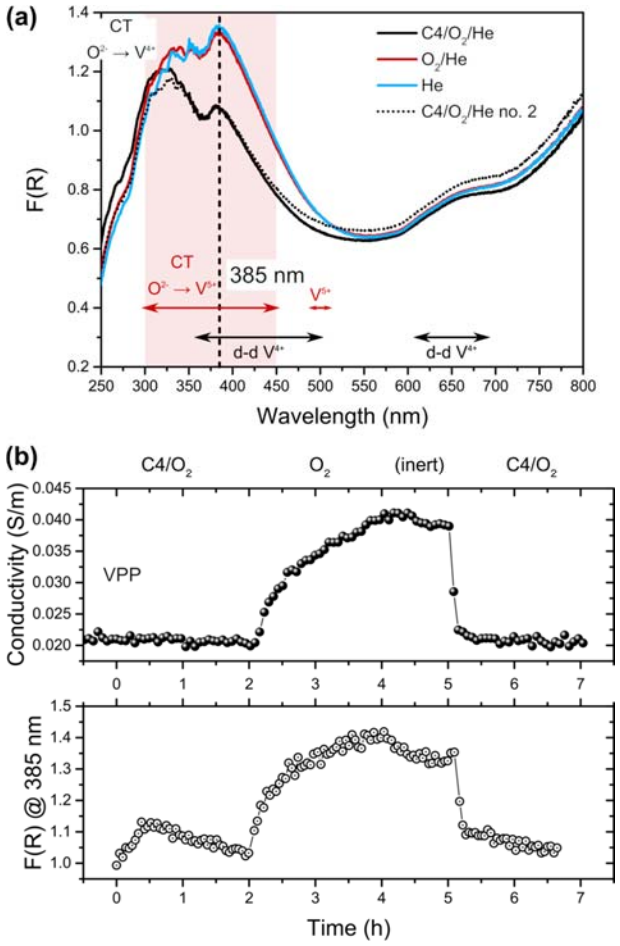

Figure S9. (a) DR-UV-Vis spectra of VPP recorded at 400 °C in different gas feeds (average spectra); **(b)** comparison of MCPT conductivity and absorption at 385 nm as time on stream plots in different gas feeds.

The absorption bands of VPP between 250 and 500 nm are due to ligand-to-metal charge transfer transitions. The O^{2-}–V^{4+} CT band occurs below 300 nm[23-26] and overlaps with the LMCT band of O^{2-}–V^{5+} that appears at a lower energy[23, 25, 27-28] exhibiting a maximum at about 385 nm as indicated in Figure S9 (a). In addition, some authors have reported a contribution of the energetically highest lying d-d transition of V^{4+} to this region.[24, 27] The following d-d transition can also be seen in the spectra between 600 and 700 nm.[24-28]

The Kubelka-Munk function at 385 nm increased upon oxidation of VPP in the 20% O_2 in He gas feed indicating a higher amount of V^{5+}. The subsequent 100% He feed was found to be inert in line with the 100% nitrogen gas feed in the MCPT conductivity measurements, i.e. no change of the V oxidation state was observed in this gas feed. The redox response of VPP was found to be reversible, which can be seen by the decrease of F(R) at 385 nm (i.e. of the oxidation state) upon returning to the reaction gas feed, see the dotted line in Figure S9 (a). In Figure S9 (b) the electrical conductivity of VPP is compared to the Kubelka-Munk function at 385 nm at 400 °C in the different gas feeds. It can be seen that both curves follow the same trends as a function of time on stream. The MCPT conductivity changes can thus be attributed to the reversible oxidation/reduction of vanadium (occupation of V 3d states) like in the case of V_2O_5. This correlation is clearer in the case of VPP, because for V_2O_5 the absorption bands of V^{4+} lie in the IR region and in the DR-UV-Vis spectra only changes in the "baseline" below the absorption edge were detected.

The DR-UV-Vis spectra of V_2O_5 in different gas feeds are shown in Figure S10 as Kubelka-Munk function F(R) with time on stream at 400 °C. The absorption at 775 nm is indicated by the dashed line.

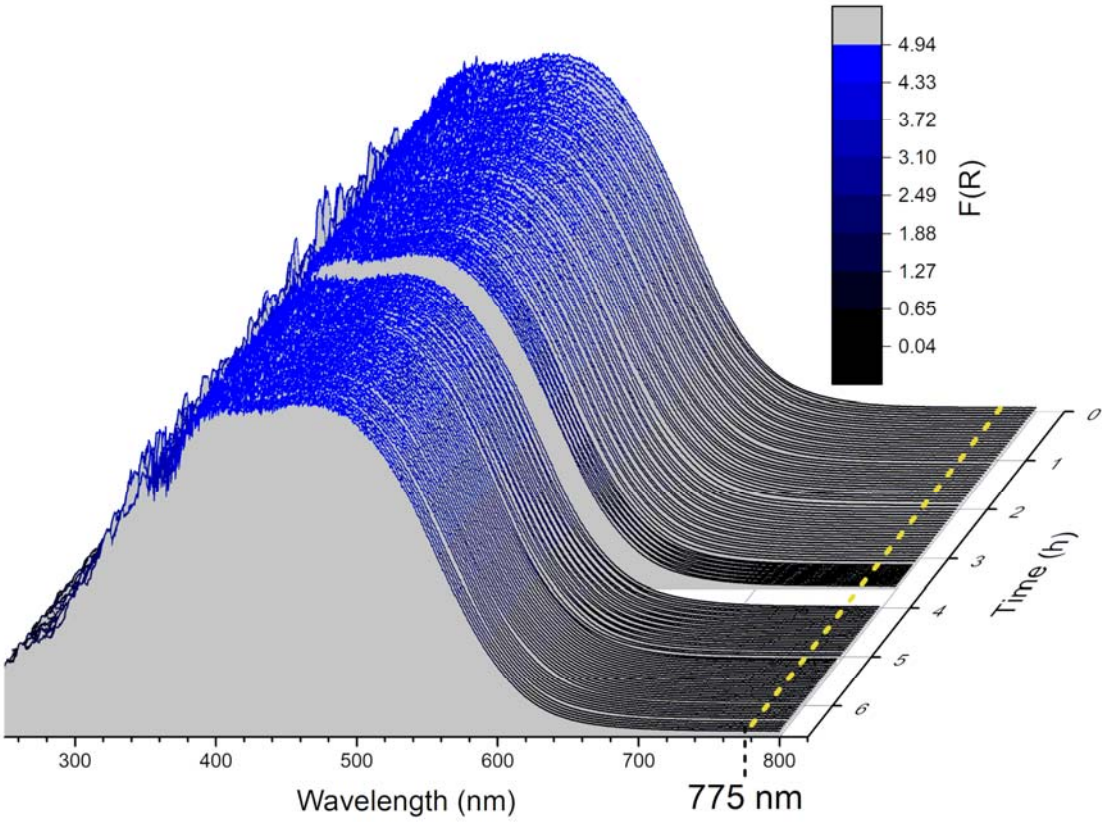

Figure S10. DR-UV-Vis spectra of V_2O_5 recorded at 400 °C in different gas feeds (2% C_4H_{10} / 20% O_2 in He ; 20% O_2 in He ; 100% He ; 2% C_4H_{10} / 20% O_2 in He). The evolution of Kubelka-Munk function F(R) at 775 nm is indicated by the dashed line.

The DR-UV-Vis spectra of VPP as Kubelka-Munk function F(R) with time on stream at 400 °C in different gas feeds are shown in Figure S11 (a) together with a schematic presentation of the three d-d transitions of the vanadyl ion in approximate local C_{4v} symmetry in Figure S11 (b).

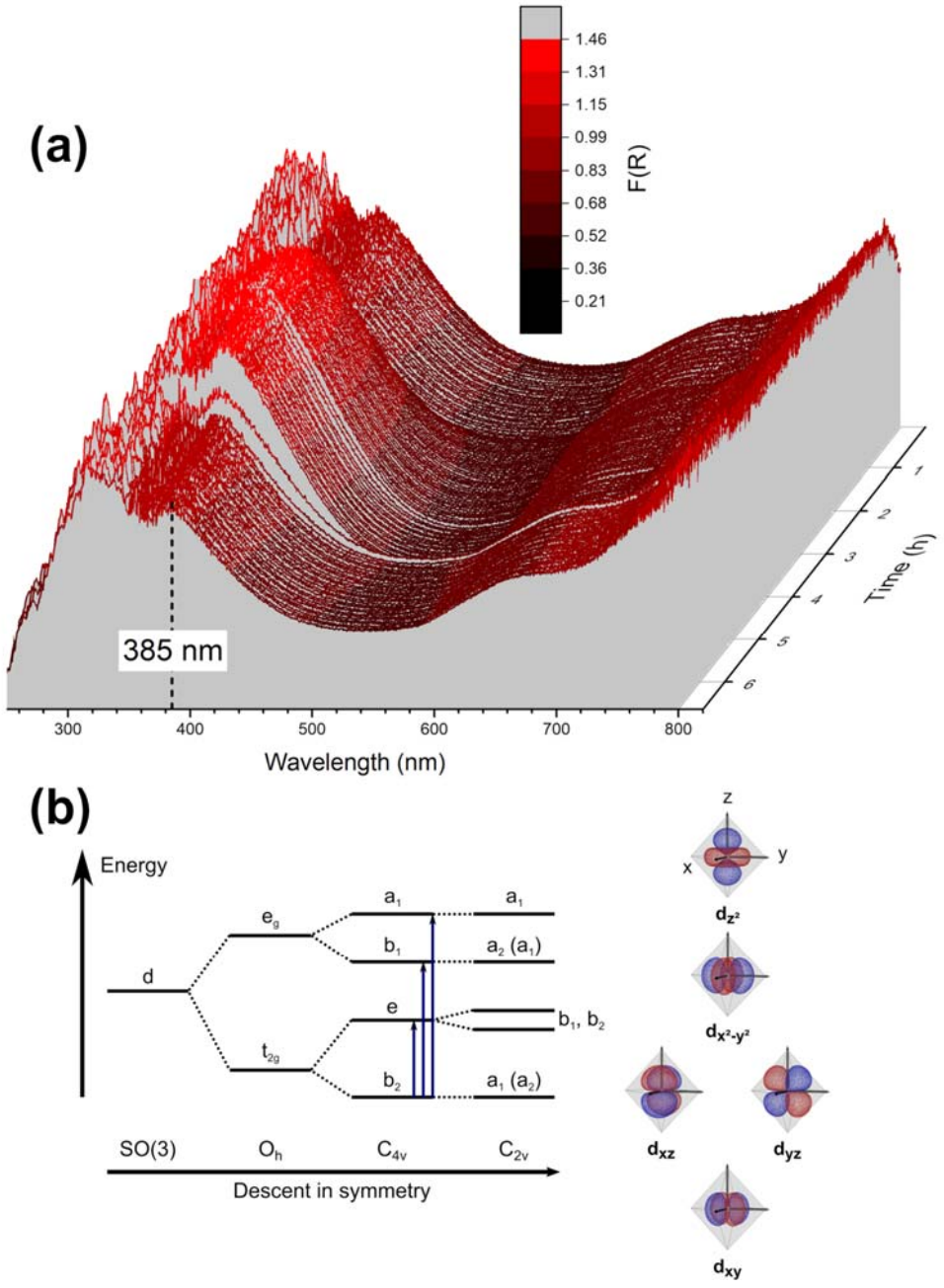

Figure S11. (a) DR-UV-Vis spectra of VPP recorded at 400 °C in different gas feeds (2% C_4H_{10} / 20% O_2 in He ; 20% O_2 in He ; 100% He ; 2% C_4H_{10} / 20% O_2 in He) and evolution of Kubelka-Munk function F(R) at 385 nm. **(b)** Scheme of the three d-d transitions of the vanadyl ion in approximate local C_{4v} symmetry showing the often-used nomenclature based on the irreducible representations in the C_{4v} group.

Temperature Dependence of Conductivity and Permittivity

The experimental procedure of the temperature dependent MCPT measurements is shown for the example of V_2O_5 measured in 20% O_2 in N_2 in Figure S12 in terms of the Q-factor change at different temperatures.

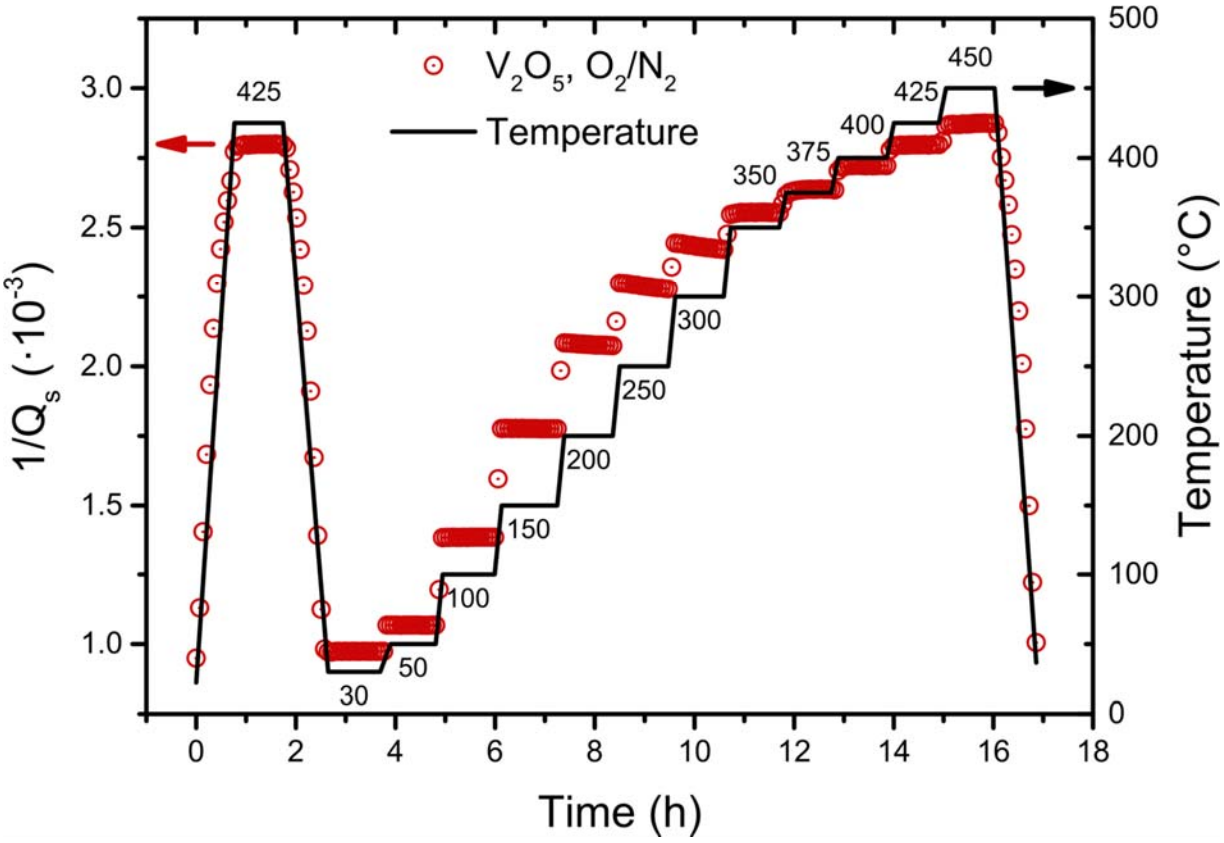

Figure S12. Experimental procedure of temperature dependent MCPT measurements: change of reciprocal Q-factor ($1/Q_s$) of V_2O_5-loaded microwave resonator (~3 GHz; TM_{010}) as a function of time in 20% O_2 in N_2, and corresponding temperatures from 30 to 450 °C, which are also indicated by the numbers.

The temperature dependent MCPT measurements of V_2O_5 in the different gas feeds (2% *n*-butane / 20% O_2 in N_2, 20% O_2 in N_2, and 100% N_2) are shown in Figure S13 in terms of the

reciprocal Q-factor change and the resonant frequency shift compared to the empty cavity measurement.

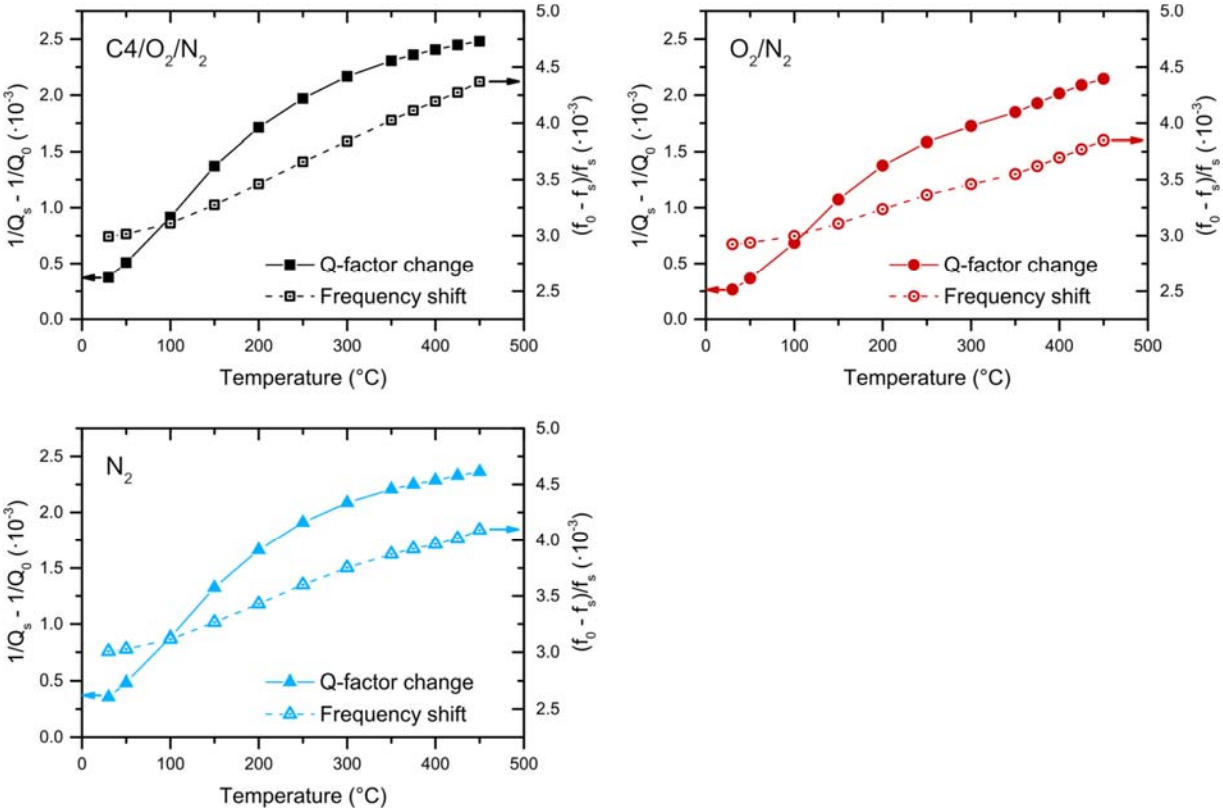

Figure S13. MCPT raw data of V_2O_5 (subscript "s") in different gas feeds (2% *n*-butane / 20% O_2 in N_2, 20% O_2 in N_2, 100% N_2) with respect to empty measurement (subscript "0"): change in reciprocal Q-factor ($1/Q_s - 1/Q_0$) and shift in resonant frequency ($[f_0 - f_s]/f_s$) as a function of temperature.

The corresponding plot of the temperature dependent MCPT measurements of VPP in the different gas feeds is presented in Figure S14.

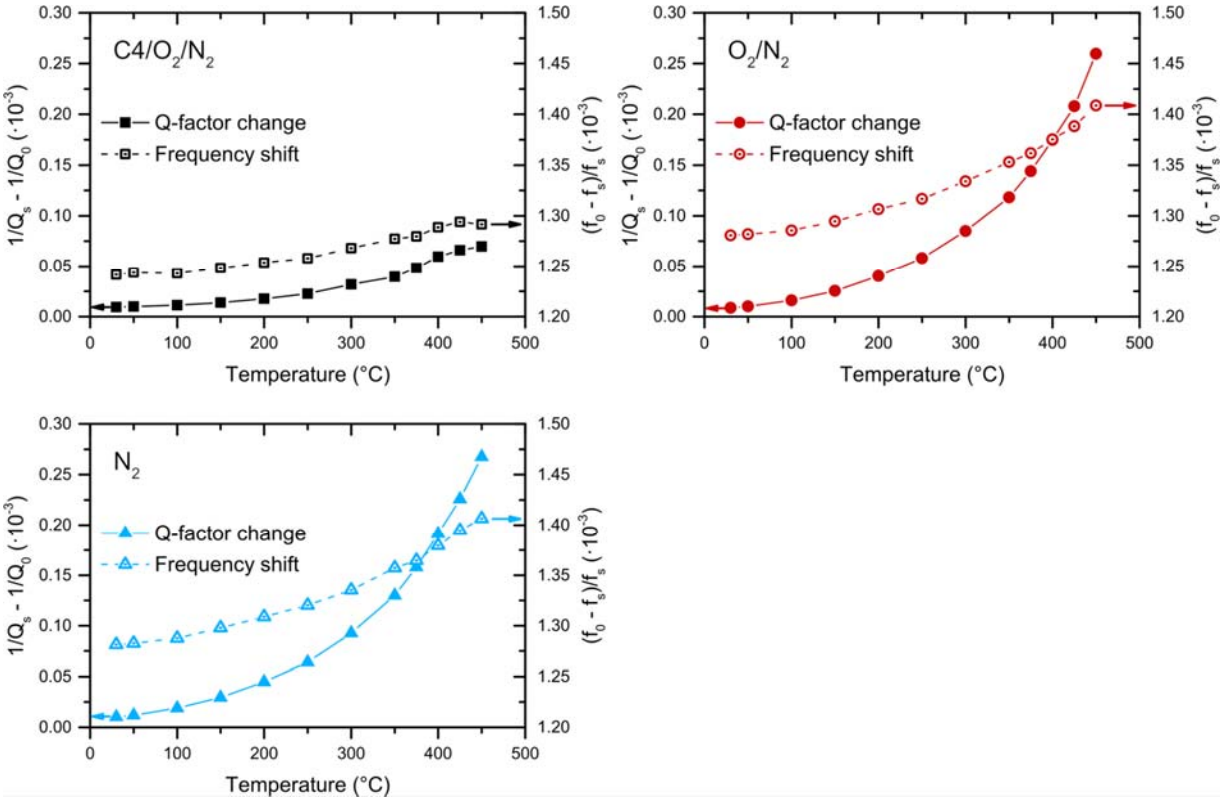

Figure S14. MCPT raw data of VPP (subscript "s") in different gas feeds (2% *n*-butane / 20% O_2 in N_2, 20% O_2 in N_2, 100% N_2) with respect to empty measurement (subscript "0"): change in reciprocal Q-factor ($1/Q_s - 1/Q_0$) and shift in resonant frequency ($[f_0 - f_s]/f_s$) as a function of temperature.

Figure S13 and Figure S14 show that the reciprocal Q-factor change of V_2O_5 first increased until about 200 °C, but then the increase levelled off, whereas the reciprocal Q-factor change of VPP kept rising. The resonant frequency shift of both samples was also increasing with temperature, however, to a smaller extent.

At first glance there seems to be a similarity between the shape of the reciprocal Q-factor change of V_2O_5 as a function of temperature and the reported depolarization peak,[29-30] still it should be emphasized that we are showing a plot of $(1/Q_s - 1/Q_0)$ *vs.* T in contrast to the logarithmic plots as a function of the reciprocal temperature that are found in literature, because,

in fact, we observed still rather small changes as compared to the increase in the reciprocal Q-factor change over several orders of magnitude (e.g. 10^{-5} to 10^{-2}) that was reported in literature.[29] This is also in line with the finding that neither V_2O_5 nor VPP reached the intrinsic conduction regime in the investigated temperature range (30 to 450 °C), as expected given the rather large band gaps (about 2 eV for V_2O_5).[17-18] In addition, the resonant frequency shift also showed rather small changes with temperature, yet it is not independent of temperature, which would occur upon reaching the high conductivity region above the depolarization crossover.[31]

In order to be able to better compare our measurements to literature, Figure S13 is plotted again as semi-logarithmic curve of the temperature dependent MCPT measurements of V_2O_5 as a function of $1/T$ in Figure S15.

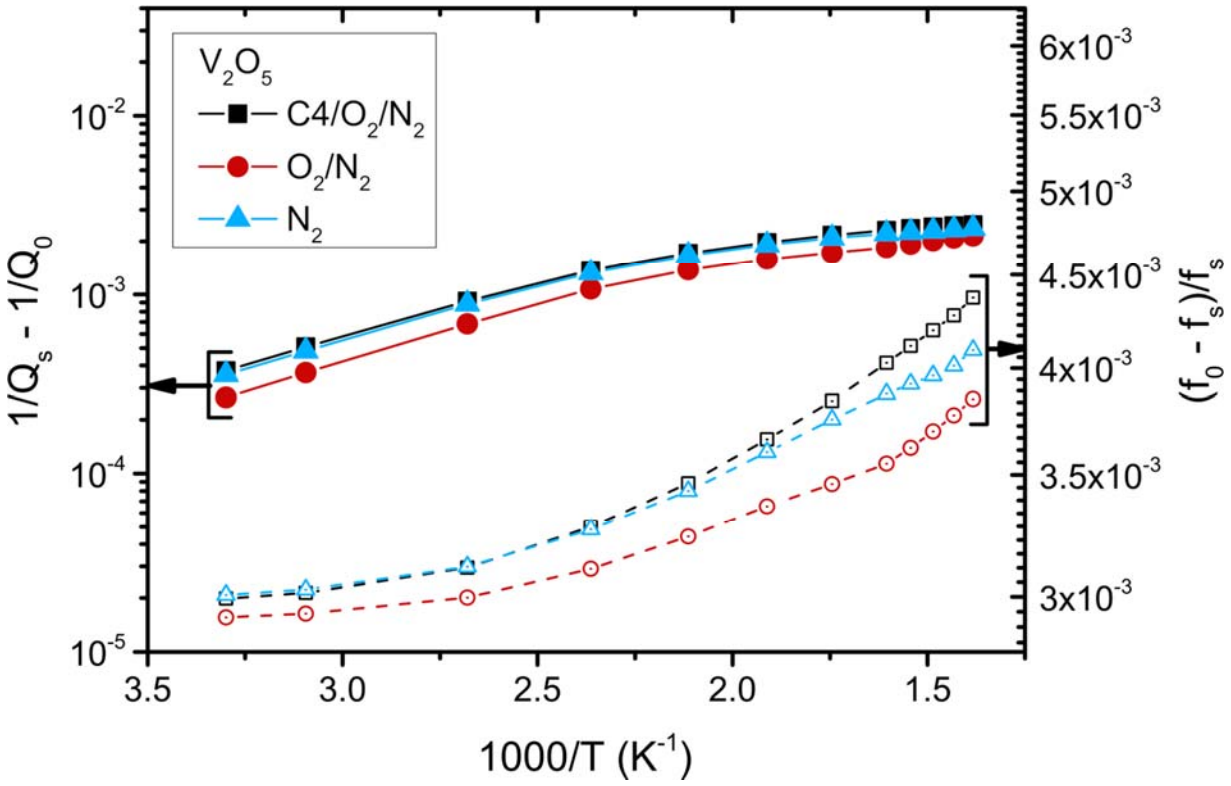

Figure S15. Reciprocal Q-factor change and resonant frequency shift of V_2O_5 in different gas feeds as semi-logarithmic plot vs. $1/T$.

It is therefore assumed that the measurements of both V_2O_5 and VPP were conducted in the low-conductivity region of the depolarization regime, in which case the resonant frequency shift is proportional to the real part of the sample's permittivity and the change in the reciprocal Q-factor is related to the imaginary part of the permittivity.[29, 32-33]

Further support for this assumption is given by a comparison of the resonant frequency shift with the cavity filling factor ($A\ (V_s/V_c)$) divided by the depolarization factor "N"[29]

$$\frac{f_0 - f_s}{f_0} \ll A\frac{V_s}{V_c}\frac{1}{N} \tag{4}$$

which yields a value of $1.8 \cdot 10^{-2}$ with an estimated maximum depolarization factor of 0.1 (for a cylinder of 1.5 mm radius and 10 mm height)[31, 33-34] compared to a much smaller frequency shift

of V_2O_5 of $3.1 \cdot 10^{-3}$ at 400 °C in 2% *n*-butane / 20% O_2 in N_2 (~3 GHz, TM_{010}), and of VPP of $1.3 \cdot 10^{-3}$ under the same conditions. It is indeed often assumed that N is close to zero.[35] It may be noted that in this case, with the demonstrated validity of the microwave cavity perturbation equations[32] used in this work, also the condition[33]

$$\varepsilon'' < \varepsilon' - 1 + \frac{1}{N} \tag{5}$$

is satisfied with the determined powder conductivities of V_2O_5 and VPP of ε_p'' (V_2O_5) = 0.43 < ε_p' (V_2O_5) = 2.7 (σ_p (V_2O_5) = 0.077 S/m) and of ε_p'' (VPP) = 0.016 < ε_p' (VPP) = 1.7 (σ_p (VPP) = $2.8 \cdot 10^{-3}$ S/m), respectively. The above-mentioned depolarization peak should occur at much higher imaginary permittivities at $\varepsilon'' = \varepsilon' - 1 + 1/N$.[33]

Taken together, there is a strong probability that the resonant frequency shift can be directly related to the real part of the permittivity of V_2O_5 or VPP and hence to dielectric relaxation and the change in the reciprocal Q-factor to the imaginary part of the permittivity, which is then used to calculate the conductivity of V_2O_5 or VPP.

The temperature dependence of the thus determined conductivities was then further investigated. Figure S16 shows the conductivity and complex permittivity of V_2O_5 and VPP as a function of temperature from 30 to 450 °C in the different gas feeds 2% *n*-butane / 20% O_2 in N_2, 20% O_2 in N_2, and 100% N_2. Both the initial values are shown upon reaching the temperature and the steady-state values, which are average values after 1 hour at the respective temperature. Both samples were previously treated at 425 °C in the different gas feeds in order to remove adsorbates like water.

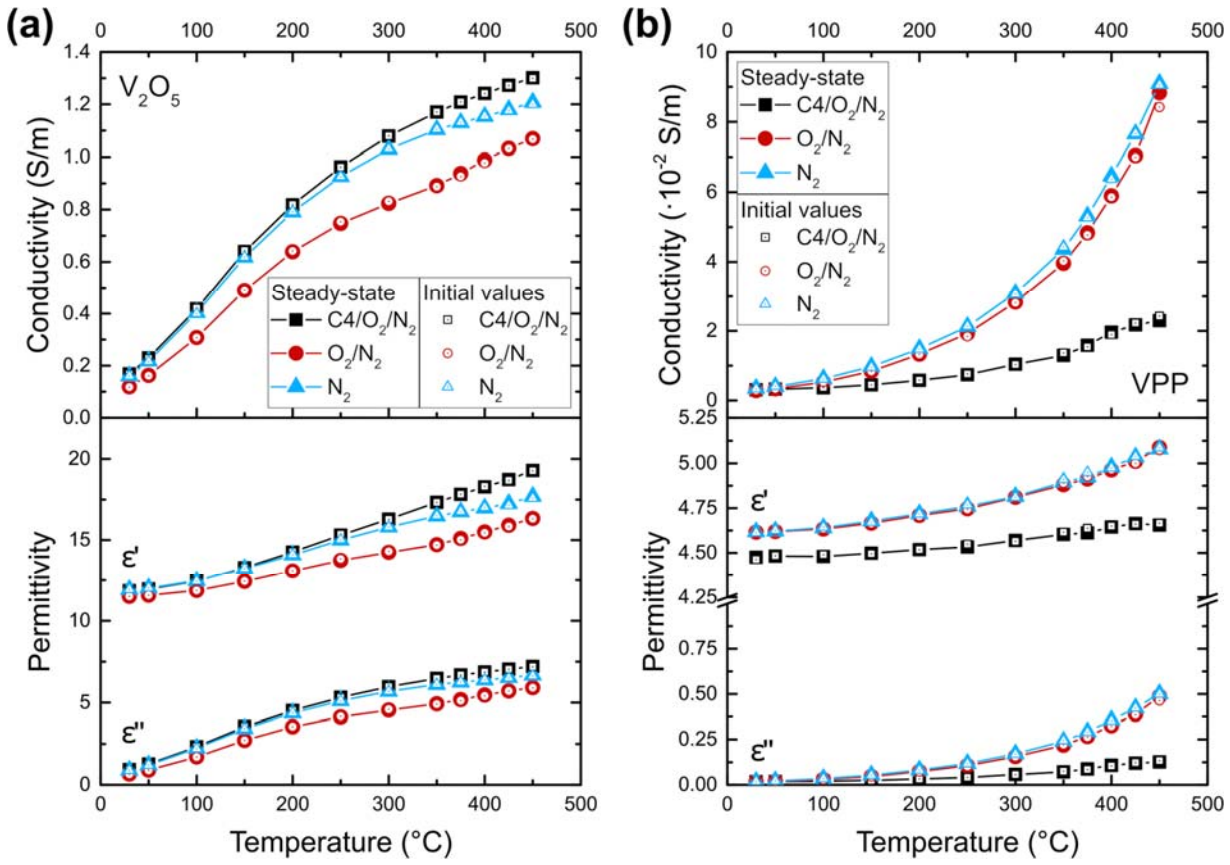

Figure S16. Temperature dependence of conductivity and complex permittivity in different gas feeds: **(a)** V_2O_5, **(b)** VPP. Both initial values after reaching a temperature (empty symbols) and steady-state values (filled symbols) are shown.

Already in the conductivity *versus* temperature curves in Figure S16, differences between the two samples can be seen. First of all, V_2O_5 exhibited an initial steep increase in conductivity below 200 °C, which levelled off at higher temperatures. In contrast to this, the conductivity of VPP started to increase significantly only above ~200 °C. Moreover, the comparison of the different gas feeds, $C_4H_{10}/O_2/N_2$, O_2/N_2, and N_2, revealed significant differences for VPP between the reaction gas feed (black squares in Figure S16 (b)) and the other gas feeds. The conductivity of V_2O_5 in Figure S16 (a) also followed the trends from before, i.e. a decrease of the conductivity with increasing oxidizing potential of the gas atmosphere $\sigma(C_4H_{10}/O_2/N_2) > \sigma(N_2) >$

$\sigma(O_2/N_2)$. However, these gas phase dependent conductivity differences in the high temperature region were much more pronounced in VPP, in particular in the reaction gas feed. This is in line with the generally observed greater relative conductivity changes of VPP in different gas feeds. The initial conductivity (empty symbols in Figure S16) and steady-state values (filled symbols) were found to be essentially the same. The permittivity of the samples likewise increased with temperature.

In order to investigate the charge transport mechanism in V_2O_5 and VPP, the temperature dependence of their conductivities was analyzed using different conduction models on the basis of semi-logarithmic conductivity *vs.* of $1/T$ plots, which are shown in Figure S17 for both V_2O_5 and VPP in the different gas feeds.

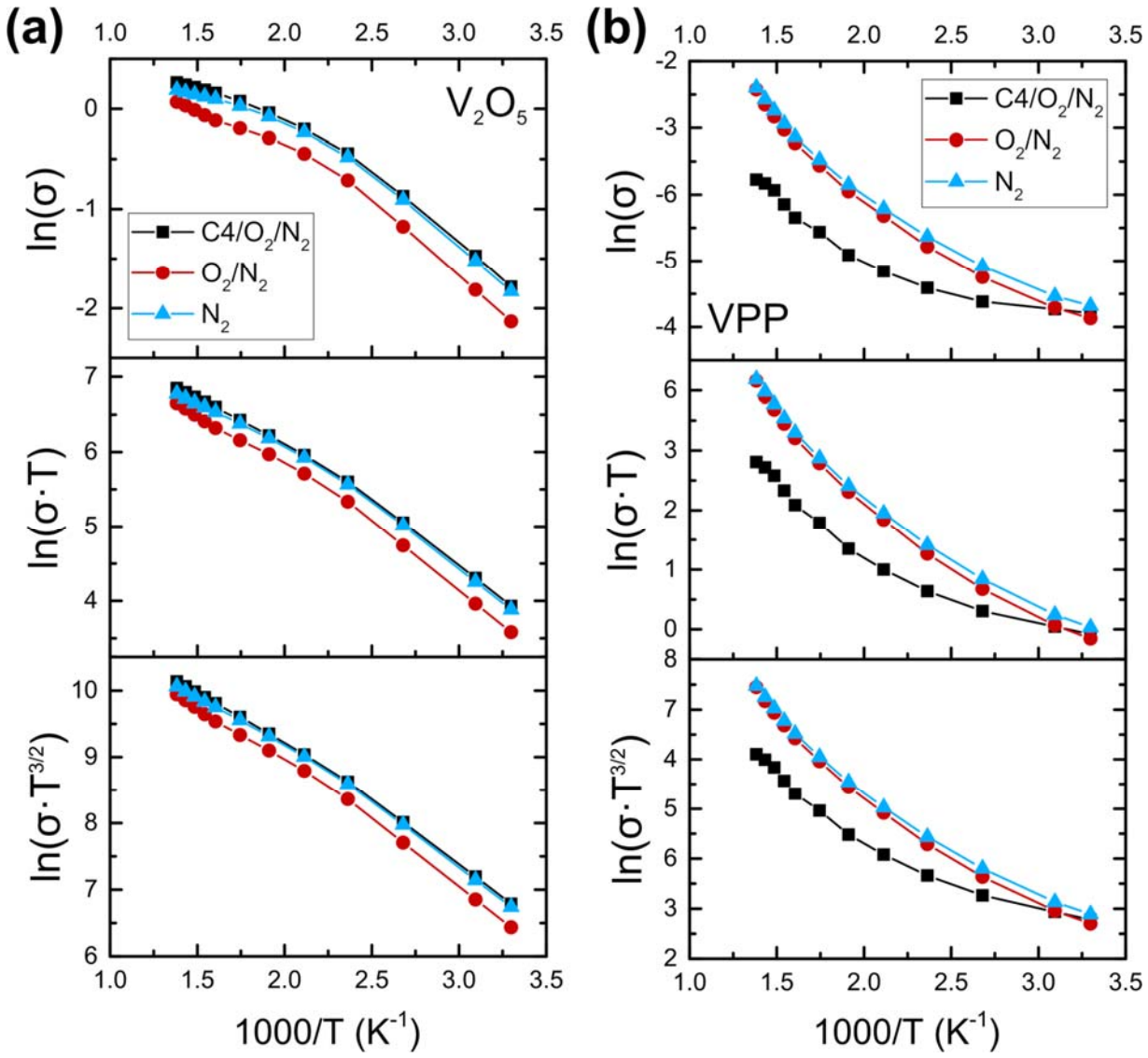

Figure S17. Determination of apparent activation energies of conduction of V_2O_5 **(a)** and of VPP **(b)** in different gas feeds (2% *n*-butane / 20% O_2 in N_2, 20% O_2 in N_2, 100% N_2) according to different models (at 3 GHz, TM_{010} mode).

The apparent activation energies of conduction were determined from the slopes in the linear regimes in Figure S17, where a low-temperature regime (≤ 100-150 °C) and a high temperature regime (350 to 450 °C) was distinguished for V_2O_5 and VPP. The results are presented in Figure S18.

The comparison to absolute literature values for the apparent activation energies of conduction should be read with care given that different samples and methods (single crystals and polycrystalline samples, DC and AC methods until 1 MHz as well as contact-less measurements based on the microwave cavity perturbation technique at 3 GHz in the present study) and sometimes different temperature regimes were studied. A lower activation energy should be measured at higher frequencies ω, as was pointed out by Eichelbaum *et al.*,[36] according to[36-37]

$$\sigma(\omega) = \sigma_{\mathrm{DC}} + A\omega^{s} \quad \Rightarrow \quad E_c = k_B T \cdot [\ln\sigma_0 - \ln(A\omega^{s})] \ . \tag{6}$$

Here, the frequency dependence of the conductivity is given in terms of a frequency-independent part (σ_{DC}) and a second part that shows a power law behavior, where the exponent s is usually close to one, and A is a parameter.[36-37] Still, we found a satisfactory agreement with literature values not only regarding the qualitative trends of the two samples, V_2O_5 and VPP, but also regarding the absolute apparent activation energies when keeping the expected decrease of the apparent activation energy at higher operating frequencies in mind.

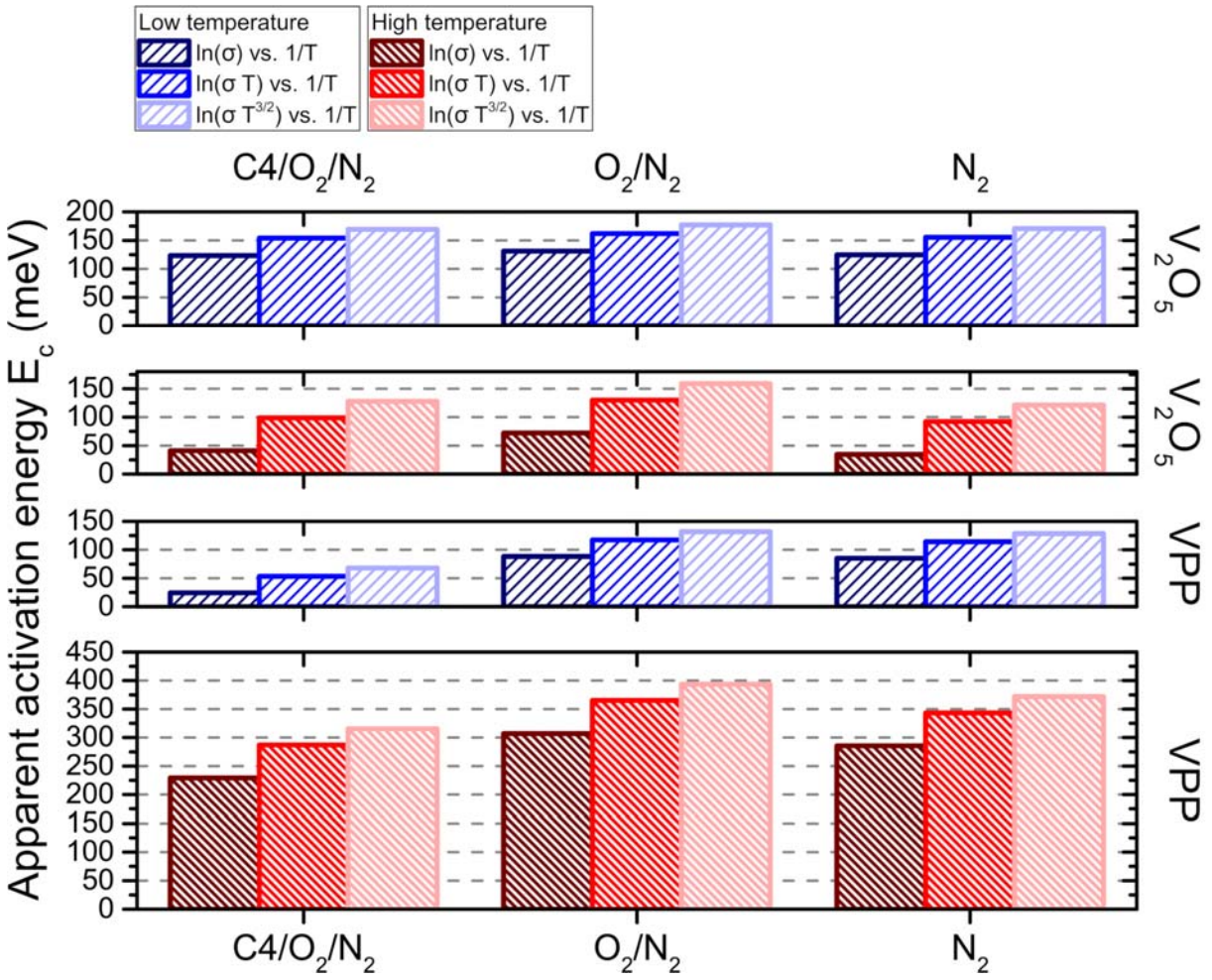

Figure S18. Apparent activation energies of conduction of V_2O_5 compared to VPP (from Figure S17). The activation energies in the low temperature range in blue (30 to 100 °C for VPP or to 150 °C for V_2O_5) and in the high temperature range in red (350 to 450 °C) are shown in different gas feeds (2% *n*-butane / 20% O_2 in N_2, 20% O_2 in N_2, 100% N_2) and using different conduction models.

It can be seen in Figure S18 that the activation energies increased when using different models, but the trends in the different gas feeds were conserved, i.e. V_2O_5 showed the highest activation energy in both the low temperature and the high temperature regime in the 20% O_2 in N_2 gas feed, which was also observed for VPP, where, however, the lowest activation energy was always found in the reaction gas feed. Figure S18 also clearly shows the much higher apparent

activation energies of conduction of VPP in the catalytically relevant high temperature regime compared to V_2O_5.

In addition to the apparent activation energies of conduction, the temperature dependence of the *n*-butane oxidation over V_2O_5 and VPP was investigated from the *operando* MCPT measurements in 2% *n*-butane / 20% O_2 in nitrogen. Figure S19 presents the Arrhenius plots of the *n*-butane consumption rates as a function of the reciprocal temperature, where the slopes were used for the determination of the apparent energies of the reaction (E_a).

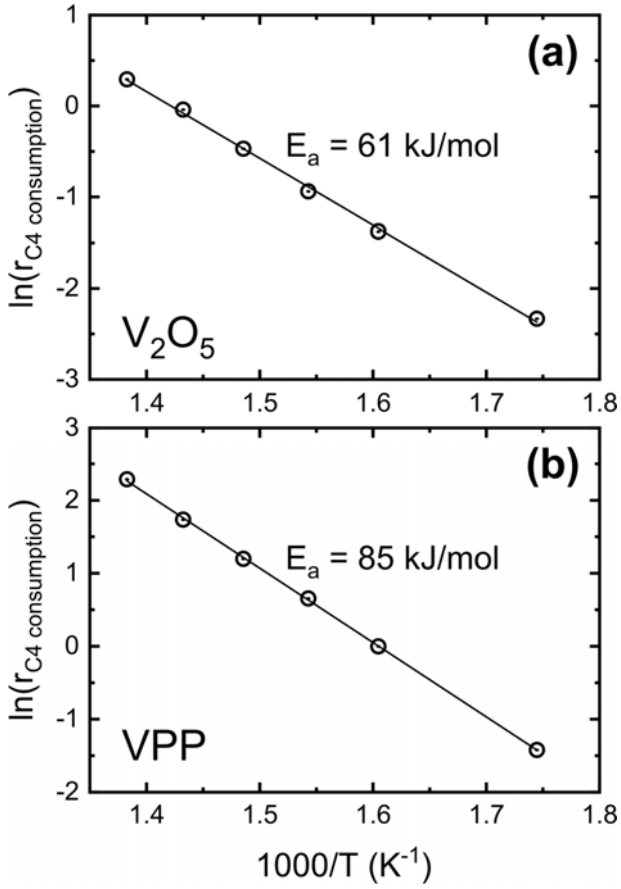

Figure S19. Arrhenius plots for determination of apparent activation energies of *n*-butane oxidation E_a **(a)** over V_2O_5 and **(b)** over VPP from temperature-dependent operando MCPT measurements in 2% *n*-butane / 20% O_2 in N_2. The natural logarithm of the overall rate of *n*-butane consumption (in mmol g^{-1} h^{-1}) is shown as a function of the reciprocal temperature.

The linear fits of the Arrhenius plots yielded apparent activation energies of *n*-butane oxidation of 61 kJ/mol or 0.63 eV for V_2O_5 and 85 kJ/mol or 0.88 eV for VPP (R^2 = 0.9982 and 0.9997 for V_2O_5 and for VPP, respectively). For VPO catalysts different values were reported in the literature ranging from ~54 to 99 kJ/mol with a decreasing activation energy with an oxidation treatment of the catalysts,[38] compare for instance to 71 – 79 kJ/mol found by Zhang-Lin *et al*.[39] or to 88 kJ/mol by Wang and Barteau.[40]

References

1. Eichelbaum, M.; Hävecker, M.; Heine, C.; Karpov, A.; Dobner, C.-K.; Rosowski, F.; Trunschke, A.; Schlögl, R. The Intimate Relationship between Bulk Electronic Conductivity and Selectivity in the Catalytic Oxidation of n-Butane. *Angew. Chem. Int. Ed.* **2012**, *51*, 6246-6250.

2. Heenemann, M.; Heine, C.; Hävecker, M.; Trunschke, A.; Schlögl, R. Influence of Steam on a Vanadyl Pyrophosphate Catalyst During Propane Oxidation. *J. Phys. Chem. B* **2018**, *122*, 695-704.

3. Haber, J.; Witko, M.; Tokarz, R. Vanadium Pentoxide I. Structures and Properties. *Appl. Catal., A* **1997**, *157*, 3-22.

4. Heine, C.; Girgsdies, F.; Trunschke, A.; Schlögl, R.; Eichelbaum, M. The Model Oxidation Catalyst α-V_2O_5: Insights From Contactless In Situ Microwave Permittivity and Conductivity Measurements. *Appl. Phys. A: Mater. Sci. Process.* **2013**, *112*, 289-296.

5. Blum, R. P.; Niehus, H.; Hucho, C.; Fortrie, R.; Ganduglia-Pirovano, M. V.; Sauer, J.; Shaikhutdinov, S.; Freund, H. J. Surface Metal-Insulator Transition on a Vanadium Pentoxide (001) Single Crystal. *Phys. Rev. Lett.* **2007**, *99*, 226103.

6. Colpaert, M. N.; Clauws, P.; Fiermans, L.; Vennik, J. Thermal and Low Energy Electron Bombardment Induced Oxygen Loss of V_2O_5 Single Crystals: Transition into V_6O_{13}. *Surf. Sci.* **1973**, *36*, 513-525.

7. Su, D. S.; Schlögl, R. Thermal Decomposition of Divanadium Pentoxide V_2O_5: Towards a Nanocrystalline V_2O_3 Phase. *Catal. Lett.* **2002**, *83*, 115-119.

8. Wu, Q.-H.; Thissen, A.; Jaegermann, W.; Liu, M. Photoelectron Spectroscopy Study of Oxygen Vacancy on Vanadium Oxides Surface. *Appl. Surf. Sci.* **2004**, *236*, 473-478.

9. Naguib, H. M.; Kelly, R. On the Increase in the Electrical Conductivity of MoO_3 and V_2O_5 Following Ion Bombardment. Studies on Bombardment-Enhanced Conductivity-I. *J. Phys. Chem. Solids* **1972**, *33*, 1751-1759.

10. Sanchez, C.; Henry, M.; Grenet, J. C.; Livage, J. Free and Bound Polarons in Vanadium Pentoxide. *J. Phys. C: Solid State Phys.* **1982**, *15*, 7133-7141.

11. Clauws, P.; Vennik, J. Optical Absorption of Defects in V_2O_5 Single Crystals: As-Grown and Reduced V_2O_5. *Phys. Status Solidi B* **1974**, *66*, 553-560.

12. Gillis, E.; Boesman, E. E. P. R.-Studies of V_2O_5 Single Crystals. I. Defect Centres in Pure, Non-stoichiometric Vanadium Pentoxide. *Phys. Status Solidi B* **1966**, *14*, 337-347.

13. Heber, M.; Grünert, W. Application of Ultraviolet Photoelectron Spectroscopy in the Surface Characterization of Polycrystalline Oxide Catalysts. 2. Depth Variation of the Reduction

Degree in the Surface Region of Partially Reduced V_2O_5. *J. Phys. Chem. B* **2000**, *104*, 5288-5297.

14. Tokarz-Sobieraj, R.; Witko, M.; Gryboś, R. Reduction and Re-Oxidation of Molybdena and Vanadia: DFT Cluster Model Studies. *Catal. Today* **2005**, *99*, 241-253.

15. Vanhaelst, M.; Clauws, P. EPR Spectrum of the Oxygen Vacancy in Single Crystals V_2O_5. *Phys. Status Solidi B* **1978**, *87*, 719-723.

16. Perlstein, J. H. A Dislocation Model for Two-Level Electron-Hopping Conductivity in V_2O_5: Implications for Catalysis. *J. Solid State Chem.* **1971**, *3*, 217-226.

17. Shin, S.; Suga, S.; Taniguchi, M.; Fujisawa, M.; Kanzaki, H.; Fujimori, A.; Daimon, H.; Ueda, Y.; Kosuge, K.; Kachi, S. Vacuum-Ultraviolet Reflectance and Photoemission Study of the Metal-Insulator Phase Transitions in VO_2, V_6O_{13}, and V_2O_3. *Phys. Rev. B* **1990**, *41*, 4993-5009.

18. Wang, L.; Maxisch, T.; Ceder, G. Oxidation Energies of Transition Metal Oxides within the GGA+U Framework. *Phys. Rev. B* **2006**, *73*, 195107.

19. Fait, M. J. G.; Abdallah, R.; Linke, D.; Kondratenko, E. V.; Rodemerck, U. A Novel Multi-Channel Reactor System Combined with Operando UV/Vis Diffuse Reflectance Spectroscopy: Proof of Principle. *Catal. Today* **2009**, *142*, 196-201.

20. Gao, X.; Jehng, J.-M.; Wachs, I. E. In Situ UV–vis–NIR Diffuse Reflectance and Raman Spectroscopic Studies of Propane Oxidation over ZrO_2-Supported Vanadium Oxide Catalysts. *J. Catal.* **2002**, *209*, 43-50.

21. Herrmann, J.-M.; Vernoux, P.; Béré, K. E.; Abon, M. In Situ Study of Redox and of p-Type Semiconducting Properties of Vanadyl Pyrophosphate and of V–P–O Catalysts during the Partial Oxidation of n-Butane to Maleic Anhydride. *J. Catal.* **1997**, *167*, 106-117.

22. Morrison, S. R. *The Chemical Physics of Surfaces*, 1 ed.; Plenum Press: New York, 1977.

23. Aït-Lachgar, K.; Abon, M.; Volta, J. C. Selective Oxidation of n-Butane to Maleic Anhydride on Vanadyl Pyrophosphate. *J. Catal.* **1997**, *171*, 383-390.

24. Bordes, E.; Courtine, P. Some Selectivity Criteria in Mild Oxidation Catalysis: V-P-O Phases in Butene Oxidation to Maleic Anhydride. *J. Catal.* **1979**, *57*, 236-252.

25. Cavani, F.; De Santi, D.; Luciani, S.; Löfberg, A.; Bordes-Richard, E.; Cortelli, C.; Leanza, R. Transient Reactivity of Vanadyl Pyrophosphate, the Catalyst for *n*-Butane Oxidation to Maleic Anhydride, in Response to *In-Situ* Treatments. *Appl. Catal., A* **2010**, *376*, 66-75.

26. Wang, F.; Dubois, J.-L.; Ueda, W. Catalytic Performance of Vanadium Pyrophosphate Oxides (VPO) in the Oxidative Dehydration of Glycerol. *Appl. Catal., A* **2010**, *376*, 25-32.

27. Loukah, M.; Coudurier, G.; Vedrine, J. C.; Ziyad, M. Oxidative Dehydrogenation of Ethane on V- and Cr-Based Phosphate Catalysts. *Microporous Mater.* **1995**, *4*, 345-358.

28. Cavani, F.; Centi, G.; Manenti, I.; Trifiro, F. Catalytic Conversion of C_4 Hydrocarbons on Vanadium-Phosphorus Oxides: Factors Influencing the Selectivity in 1-Butene Oxidation. *Ind. Eng. Chem. Prod. Res. Dev.* **1985**, *24*, 221-226.

29. Bauhofer, W. Determination of Semiconductor Energy Gaps Using the Microwave Cavity Perturbation Method. *J. Phys. E: Sci. Instrum.* **1981**, *14*, 934-938.

30. Ong, N. P. Microwave Cavity-Perturbation Equations in the Skin-Depth Regime. *J. Appl. Phys.* **1977**, *48*, 2935-2940.

31. Shchegolev, I. F. Electric and Magnetic Properties of Linear Conducting Chains. *Phys. Status Solidi A* **1972**, *12*, 9-45.

32. Chen, L. F.; Ong, C. K.; Neo, C. P.; Varadan, V. V.; Varadan, V. K. *Microwave Electronics: Measurement and Materials Characterization*; John Wiley & Sons, Ltd: Chichester, West Sussex, U.K., 2004.

33. Klein, O.; Donovan, S.; Dressel, M.; Grüner, G. Microwave Cavity Perturbation Technique: Part I: Principles. *Int. J. Infrared Millimeter Waves* **1993**, *14*, 2423-2457.

34. Osborn, J. A. Demagnetizing Factors of the General Ellipsoid. *Phys. Rev.* **1945**, *67*, 351-357.

35. Grabtchak, S.; Cocivera, M. Microwave Response due to Light-Induced Changes in the Complex Dielectric Constant of Semiconductors. *Phys. Rev. B* **1998**, *58*, 4701-4707.

36. Eichelbaum, M.; Stößer, R.; Karpov, A.; Dobner, C.-K.; Rosowski, F.; Trunschke, A.; Schlögl, R. The Microwave Cavity Perturbation Technique for Contact-Free and *In Situ* Electrical Conductivity Measurements in Catalysis and Materials Science. *Phys. Chem. Chem. Phys.* **2012**, *14*, 1302-1312.

37. Jonscher, A. K. The 'Universal' Dielectric Response. *Nature* **1977**, *267*, 673-679.

38. Schuurman, Y.; Gleaves, J. T. Activation of Vanadium Phosphorus Oxide Catalysts for Alkane Oxidation. The Influence of the Oxidation State on Catalyst Selectivity. *Ind. Eng. Chem. Res.* **1994**, *33*, 2935-2941.

39. Zhang-Lin, Y.; Forissier, M.; Sneeden, R. P.; Védrine, J. C.; Volta, J. C. On the Mechanism of *n*-Butane Oxidation to Maleic Anhydride on VPO Catalysts: I. A Kinetics Study on a VPO Catalyst as Compared to VPO Reference Phases. *J. Catal.* **1994**, *145*, 256-266.

40. Wang, D.; Barteau, M. A. Kinetics of Butane Oxidation by a Vanadyl Pyrophosphate Catalyst. *J. Catal.* **2001**, *197*, 17-25.